ACS APPLIED MATERIALS & INTERFACES

Research Article

Cite This: ACS Appl. Mater. Interfaces 2019, 11, 41363−41373

www.acsami.org

# SnS Nanosheets Confined Growth by S and N Codoped Graphene with Enhanced Pseudocapacitance for Sodium-Ion Capacitors

Mingshan Wang,*,† Hao Xu,† Zhenliang Yang,‡ Hua Yang,† Anmin Peng,† Jun Zhang,† Junchen Chen,† Yun Huang,† Xing Li,*,† and Guozhong Cao*,§

†School of Materials Science and Engineering, Southwest Petroleum University, Chengdu, Sichuan 610500, P. R. China
‡Institute of Materials, China Academy of Engineering Physics, Mianyang, Sichuan 621908, P. R. China
§Department of Materials Science and Engineering, University of Washington, Seattle, Washington 98195, United States

*Supporting Information*

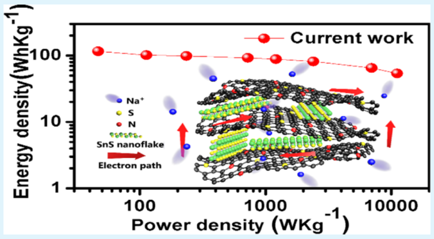

**ABSTRACT:** Layered tin monosulfide (SnS) is a promising anode material for sodium-ion batteries because of its high theoretical capacity of 1020 mA h g$^{-1}$. Its large interlayer spacing permits fast sodium-ion transport, making it a viable candidate for sodium-ion capacitors (SICs). In this work, we designed and synthesized oriented SnS nanosheets confined in graphene in the presence of poly(diallyl dimethyl ammonium chloride) by electrostatic self-assembly during hydrothermal growth. SnS nanosheets growing along (*l*00) and (0*l*0) directions are suppressed because of the confinement by graphene, which exhibit smaller thickness and particle size. These nanostructures expose abundant open edges because of the presence of Sn$^{4+}$−O, which offers rich active sites and Na$^+$ easy transport pathways. Vacancies formed at these edges along with S and N codopants in the graphitic structure synergistically promoted Na$^+$ surface adsorption/desorption. Such nanocomposites with SnS nanosheets confined by N,S codoped graphene demonstrated significantly enhanced pseudocapacitance. The SICs delivered excellent energy densities of 113 and 54 W h kg$^{-1}$ at power densities of 101 and 11 100 W kg$^{-1}$, respectively, with 76% capacity retention after 2000 cycles at 1 A g$^{-1}$.

**KEYWORDS:** *SnS, graphene, N,S co-doped, pseudocapacitive, sodium-ion capacitor*

## 1. INTRODUCTION

With the consumption of traditional fossil energy and deterioration of the environment, the development and utilization of renewable energy become extremely urgent during this century. Because of their unstable output of energy, electrochemical energy storage devices are key technologies to adjust and accelerate effective application of green energy.[1−3] Lithium-ion battery technology has made rapid development during the past decades, which has the advantages of high energy density and power density among various types of batteries.[4] However, the expensive raw materials arising from the scarcity of lithium resources seriously affected lithium-ion battery applications in the stationary largescale energy storage devices.[5−8]

Based on this situation, developing other high efficient energy storage technologies with low cost to replace the lithium-ion battery is an urgent mission for the future energy storage market. Among this, the sodium-ion battery (SIB) is considered as the most attractive storage technology because of its abundant sodium resource in nature, mature processing technology, and the similar electrochemical properties as the lithium-ion battery.[9,10] Although the storage mechanism of the lithium-ion battery is similar with the SIB, both based on alkaline ions reversibly move back and forth between cathode/anode materials. Most of the conventional lithium-ion battery materials are no longer suitable for SIB, which owing to the larger ionic size of sodium (1.02 Å) and higher standard electrode potential of sodium (≈−2.71 V vs SHE) than those of lithium. Especially for the graphitic anode materials readily insert with Li$^+$, can only intercalate a small amount of Na$^+$ for SIB.[11] As a result, a large number of new anode materials have been introduced as electrode materials for SIBs during the past few years.[12] Among various alternative anode materials of SIB, layered transition metal sulfides (cobalt sulfides,[13] molybdenum sulfides,[14] iron sulfides, etc.[15]) have caused great concern because of their unique two-dimensional layered structure and large interlayer spacing, which are beneficial for the mechanical stability because of the smaller volume changes during the cycling process. Besides, weaker M−S bonds in the metal sulfide than M−O bonds in the metal oxide can also be favorable for sodiation/desodiation process, exhibiting higher reversible capacity and initial Coulombic efficiency than some nongraphitic carbon and metal oxide anode materials for the SIB.[16] As a typical example, orthorhombic tin sulfides (SnS) have a unique two dimensional layered structure with large interlayer spaces (0.56 nm),[17] along with weak van der Waals forces between adjacent Sn−S layers, which is beneficial to Na$^+$ intercalation process. The theoretical capacity of SnS can

**Received:** August 9, 2019
**Accepted:** October 10, 2019
**Published:** October 10, 2019

DOI: 10.1021/acsami.9b14098
ACS Appl. Mater. Interfaces 2019, 11, 41363−41373

achieved to 1020 mA h $g^{-1}$, showing higher theoretical capacity than that of pristine Sn based on conversion reaction from SnS to Sn and alloying reaction from Sn to $Na_{15}Sn_4$.[18] Nevertheless, large volume expansion in the process of a large amount of $Na^+$ participating in the electrochemical reaction, inherent low electrical conductivity, loss of polysulfide and sluggish sodiation kinetics, which lead to increased decaying of capacity and poor rate performance. In order to overcome these issues, many modification strategies, such as synthesis of nanoparticles,[7,19−22] heteroatom doping to expand the interlayer spacing,[23−25] and introduction of carbon analogs,[11,26] have been investigated and evaluated. Inspired by the pervious works, constructing nanostructures for metal sulfide materials with high surface area and two-dimensional nanostructure, could shorten the ion diffusion pathway and guarantee numerous active sites for $Na^+$ diffusion and storage. As a result, SnS is considered as a promising high energy density anode material for SIBs.[19−21,27]

The sodium-ion capacitor (SIC) is a new type of hybrid capacitor, since the first research began in 2012.[28] Its working principle is to use the battery type materials of SIBs as the anode and the capacitor type material (such as active carbon) as the cathode. During the charging process, anion ions (such as $ClO_4^-$) move toward the cathode to form electrical double layers, and sodium ion migrates to the anode to produce faradaic reaction; electrons are transferred from the cathode to the anode in an external circuit.[29−34] As a result, the hybrid devices can combine the advantages of a battery and a supercapacitor by adapting their individual working manner. In addition, the hybrid devices can operate at large potential windows because two electrodes can perform at different potential ranges.[35] As a result, the sodium-ion hybrid storage system can achieve high energy density and power density simultaneously by optimizing both cathode and anode materials.[36] In order to match the rapid adsorption/desorption non-Faraday reaction process, the anode materials for sodium-ion hybrid capacitors are needed to have high electrochemical reaction kinetics. Some two dimensional metal sulfides, such as $MoSe_2$,[29] $SnS_2$.[37,38] exhibit excellent rate capability at high current density mainly because of the contribution of pseudocapacitance; meanwhile, they show excellent rate performance as the anode of SIBs. In addition, density functional theory (DFT) calculations also confirm that such metal sulfide materials exhibit pseudocapacitance from charge transfer and double layer capacitance contribution from a large surface area.[37,39,40] These unique advantages of metal sulfide materials make them potential electrode materials with high energy density to be used as SIC anodes.

Inspired by the new understanding of metal sulfide, in this work, we systematically investigated the orthorhombic SnS, with a typical layered structure and large interlayer spacing, as the anode for SICs. According to electrostatic self-assembly with poly(diallyl dimethyl ammonium chloride) (PDDA), the growth of SnS nanosheets along (*l*00) and (0*l*0) directions can be confined in the graphene with smaller thickness and particle size. This structure is preferred for $Na^+$ to intercalate along the Z-axis with open edges. Meanwhile, the open edges of SnS possess a lot of vacancies, and along with the N,S codoped graphene structure, they provide abundant active sites for $Na^+$ pseudocapacitance storage. As a result, as an anode for the SIB, the SnS/rGO exhibits much better electrochemical stability, higher rate capability, and a higher ratio of capacitance contribution in the whole capacity than that of pure SnS. As an anode material for SICs,the SnS/rGO composite presented energy densities of 113 W h $kg^{-1}$ at 101 W $kg^{-1}$ and 54 W h $kg^{-1}$ at 11 100 W $kg^{-1}$, with 76% capacity retention after 2000 cycles at 1 A $g^{-1}$.

## 2. EXPERIMENTAL SECTION

**2.1. Material Synthesis.** Graphene oxide (GO) powder (purity > 99 wt %) was purchased from Daying Juneng Technology and Development Co., Ltd. (China). The thickness of GO is 0.55−3.58 nm. The PDDA (1 wt %), $K_2SnO_3\cdot 3H_2O$ and L-cysteine were purchased from Aladdin without further purification.

**2.2. Synthesis of the SnS/rGO Composite.** The SnS/rGO composite was prepared via electrostatic self-assembly under hydrothermal treatment followed by a thermal reduction approach. In a typical procedure, 0.1 g of graphite oxide was first distributed in a 100 mL of deionized water to form uniform yellow suspension by ultrasonication for 3 h. A portion of 5 mL of PDDA solution was slowly dropped into the 50 mL of GO solution and subjected to magnetic stirring for 1 h to realize the electrostatic self-assembly process. Then, 0.3 g of $K_2SnO_3\cdot 3H_2O$ and 0.5 g of L-cysteine were dissolved in the mixture under magnetic stirring for 1 h. After that, the mixture was transferred to a 100 mL stainless steel Teflon-lined autoclave. The autoclave was sealed and the temperature was maintained at 200 °C for 24 h before cooling down to room temperature. Then, the dark green precipitation product was washed three times with deionized water and vacuum dried at 60 °C for 24 h. Then, the intermediate product was further heated to 600 °C for 2.5 h in a tube furnace under the Ar atmosphere to obtain the SnS/rGO composite. For comparison, the original SnS was prepared in the same way just without adding GO.

**2.3. Material Structural Characterization.** The morphologies and crystalline structures of SnS and SnS/rGO composites were characterized by high-resolution transmission electron microscopy (HRTEM, G2F20 S-TWIN), field-emission scanning electron microscopy (JEOL JSM7500), and X-ray diffraction (XRD, Rigaku D/Max III diffractometer with Cu K$\alpha$ radiation). The surface elemental states of the samples were characterized by X-ray photoelectron spectroscopy (XPS, Thermo Scientific ESCALAB 250Xi). The content of carbon in the composite was characterized by thermogravimetric analysis (METTLER TOLEDO TGA/SDTA851e) in air at 20 °C/min. The zeta potentials of GO-PDDA and GO suspensions were determined using a Zetasizer 3000HS (Malvern Instruments). Raman spectroscopy was determined using a Renishaw RM1000 equipped with a He−Ne laser at an excitation wavelength of 532 nm.

**2.4. Electrochemical Characterizations.** The slurry was prepared by blending the active materials with ketjen black (KB) as the conductive agent and carboxymethyl cellulose as the binder in a weight ratio of 8:1:1 to form uniform slurry. The mixture slurry was coated on a copper foil and predried at 60 °C. Then, the electrodes were further vacuum dried for 24 h before use. The typical mass loading was 1.1 ± 0.1 mg $cm^{-2}$ for each Φ14 electrode piece. In addition, we further tested the electrochemical properties of SnS/rGO of 2.3 ± 0.1 mg $cm^{-2}$ for each Φ14 electrode piece.

The electrochemical performances of SnS and SnS/rGO anodes were evaluated by testing CR2032-type half-cells, which use sodium foil as the counter electrode and the abovementioned electrode piece as the working electrode. $NaClO_4$ (1 M) dissolved in dimethyl carbonate and propylene carbonate (PC) (v/v = 1:1), by adding another 5 wt % fluoroethylene carbonate addictive were used as the electrolyte. The glass fiber (Whatman, GF/D) was used as the separator. The electrochemical stabilities of SnS and SnS/rGO were investigated by galvanostatic charge/discharge tests in the potential range 0.01−2.5 V at different current densities (NEWARE instrument). The electrochemical impedance spectroscopy (EIS) tests were conducted in a frequency ranging from 100 kHz to 10 MHz on an electrochemical workstation (Shanghai Chenhua, CHI660D). The cyclic voltammetry (CV) curves were measured at a scan rate of 0.1 mV $s^{-1}$ between 0.01 and 3 V on the same workstation.

**Scheme 1. Schematic Diagram of the Fabrication Process of the SnS/rGO Composite; First, Graphite Oxide Solution Are Modified by PDDA To Graft Positive Charges because of the $NH_2^+$ Groups of PDDA; Then, $SnO_3^{2-}$ Are Easily Wrapped on the Surface of $NH_2^+$-Modified GO and Further Adsorb L-cysteine Molecular Move around $SnO_3^{2-}$; Under the Hydrothermal Condition, L-Cysteine Are Hydrolyzed To Form $H_2S$ and $CH_3COOH$, Which React with $SnO_3^{2-}$ To Form $SnS_2$; During This Process, PDDA Functions as a Glue Molecule To Induce the Growth of Layered $SnS_2$ Distributed on the Surface of GO; Finally, at a Higher Heating Temperature, $SnS_2$ Can Be Reduced to SnS because of Sulfur Release**

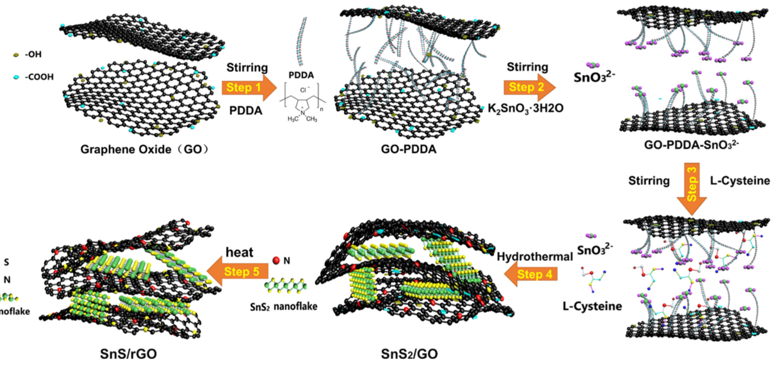

For the SICs, activated carbon (AC), KB, and polyvinylidene fluoride were mixed in the weight ratio of 7:2:1 to form a homogeneous slurry using *N*-methylpyrrolidone as the solvent. Then, the slurry was coated on an aluminum foil as the current collector. The AC//SnS/rGO hybrid capacitor was assembled by the AC electrode as the cathode and presodiated SnS/rGO as the anode with the same separator and electrolyte for SIB. The presodiated SnS/rGO electrode was cycled for 3 cycles at 0.2 A $g^{-1}$ to discharge at 0.01 V, followed by dismantling the cells. All the cells were assembled in the Ar-filled glove box with $O_2$ and $H_2O$ below 0.5 ppm. Galvanostatic charge/discharge tests of the SICs were optimized by adjusting the potential range and current densities. The energy and power density of SICs were calculated according to the following formula.[20]

$$E = \int_{t_2}^{t_1} IV\ \mathrm{d}t \tag{1}$$

$$p = \frac{E}{t} \tag{2}$$

where $V$ refers to the voltage, $I$ is the current density, and $t$ is the time of each charge/discharge cycle. The capacitance was calculated based on the gross mass of both anode and cathode materials.

## 3. RESULTS AND DISCUSSION

The synthesis procedure of the SnS/rGO composite is illustrated in Scheme 1. First, GO was modified by PDDA to change the charge of the GO surface from negative to positive. Table S1 displayed the zeta potential of GO at different pH values. The zeta potential of GO can be changed from −33.16 mV at pH = 5 to +38.74 mV after PDDA addition of 1 mg/mL. Owing to the strong cationic polyelectrolyte with the positive charge of PDDA, it can be easily adsorbed on the surface of GO through electrostatic attraction.[41,42] Then, $SnO_3^{2-}$ can be further adsorbed onto the surface of GO by the $NH_2^+$ groups of PDDA. The $SnO_3^{2-}$ ions on the surface of GO generate many nucleation sites to attract L-cysteine molecular move around them under the hydrothermal reaction process. Then, under the hydrothermal condition, L-cysteine plays as a sulfur donor to convert $SnO_3^{2-}$ to $SnS_2$. XRD patterns of hydrothermal grown samples are shown in Figure 1a, revealing hexagonal $SnS_2$ is the only crystalline phase. The main diffraction peaks are index to the JCPDS no. 23-0677. Finally, the $SnS_2$ nanosheets are converted into SnS nanosheets by annealing owing to the dissociation of $SnS_2$ by the reaction of $SnS_2(s) \overset{\Delta}{\rightarrow} SnS(s) + \frac{1}{x}S_x(g)$ at high temperature, which is in good agreement with the literature.[43]

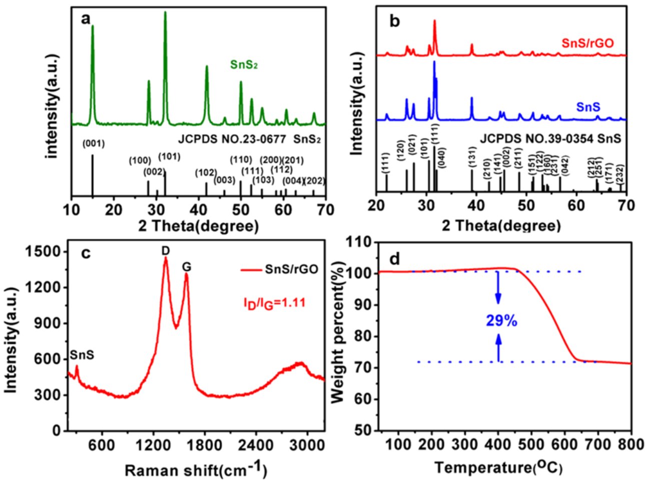

**Figure 1.** (a) XRD pattern of pure $SnS_2$ prior to heat treatment; (b) XRD patterns of SnS and SnS/rGO; (c) Raman spectra of SnS/rGO; and (d) TG curve of the SnS/rGO.

Figure 1b shows the XRD patterns of SnS and SnS/rGO samples. All main diffraction peaks can be assigned to the orthorhombic SnS in both SnS and SnS/rGO samples, which agree with the JCPDS no. 39-0354. The crystal size of SnS/rGO and SnS are further analyzed based on (040) and (002) diffraction peaks according to the Scherer equation, and the results are presented in Table S2.

The crystallite sizes of SnS/rGO along (040) and (002) are 16 and 11 nm, respectively, while those of SnS were 43 and 20 nm, indicating that the orientation growth of SnS in the SnS/rGO along (0*l*0) and (00*l*) directions are suppressed by the graphene, as reported in literature.[44] It is also worth noting that there are no characteristic diffraction peaks of rGO at 25.4° for the SnS/rGO composite,which might result from the random restacking of rGO layers.[45] The Raman spectra further certify the existence of rGO in the SnS/rGO composite. Figure 1c shows two peaks located at 1350 and 1580 $cm^{-1}$, corresponding to defects and disorders of the carbon structure (D band) and the vibration of the carbon atoms with $sp^2$

DOI: 10.1021/acsami.9b14098
ACS Appl. Mater. Interfaces 2019, 11, 41363−41373

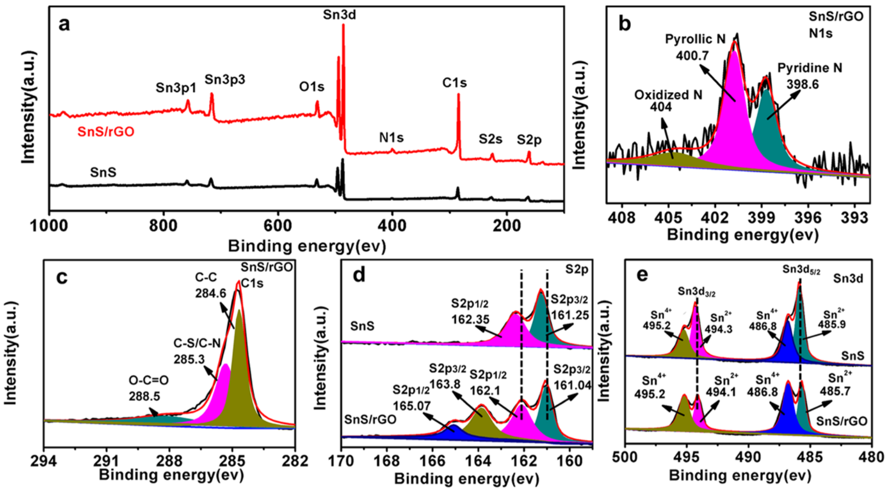

**Figure 2.** (a) XPS spectra of SnS and SnS/rGO, (b) N 1s, (c) C 1s, (d) S 2p, and (e) Sn 3d in SnS and SnS/rGO.

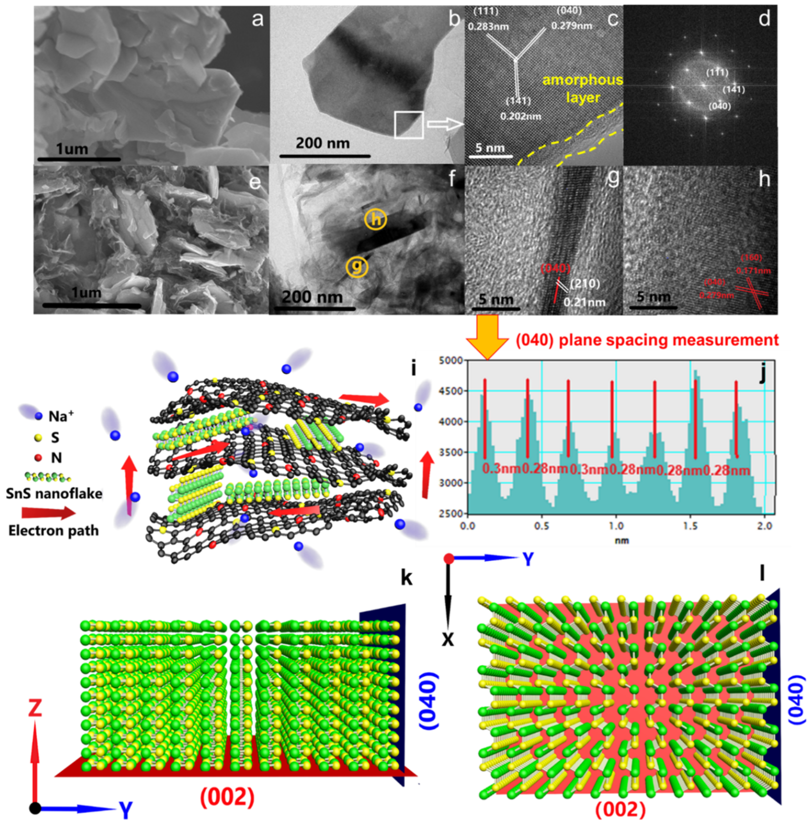

**Figure 3.** (a,e) SEM images of SnS and SnS/rGO, respectively; (b,c) TEM images of SnS; (d) the resulting fast Fourier transform pattern; (f–h) TEM images of SnS/rGO; (i) schematic diagram of the working principle of SnS/rGO; (j) (040) crystal plane spacing test; (k,l) schematic illustration of the 2-dimensional SnS structure viewed along (*l*00) and (00*l*) zone axes with inserted (002) (red plane) and (040) (blue plane) planes.

electronic configuration in a hexagonal lattice (G band), respectively.[46] Another broad peak appears at 2700 cm$^{-1}$ for the SnS/rGO composite, indicating the formation of a multilayer graphene structure.[21,47,48] The intensity of the D band is much higher than that of the G band in the SnS/rGO composite ($I_D/I_G$ = 1.11), indicating thehighly disordered structure of graphene. The content of carbon in the SnS/rGO composite was estimated by thermogravimetric analysis (Figure 1d). Considering that SnS completely converted to SnO$_2$ with no change of weight, the weight loss of the composite is assigned to the oxidation of carbon and is estimated to be 29%.

Surface chemical bonding states in the SnS/rGO composite were studied by means of XPS. As shown in Figure 2a, Sn, O, N, S, and C elements were observed in the SnS/rGO composite, with peaks at binding energies of 700–760 eV (Sn 3p), 531 eV (O 1s), 480–500 eV (Sn 3d), 390–410 eV (N 1s), 282–295 eV (C 1s), 210–240 eV (S 2s), 150–170 eV (S 2p).[46] A pronounced N 1s peak at 390–410 eV suggests the successful incorporation of the N element into the SnS/rGO

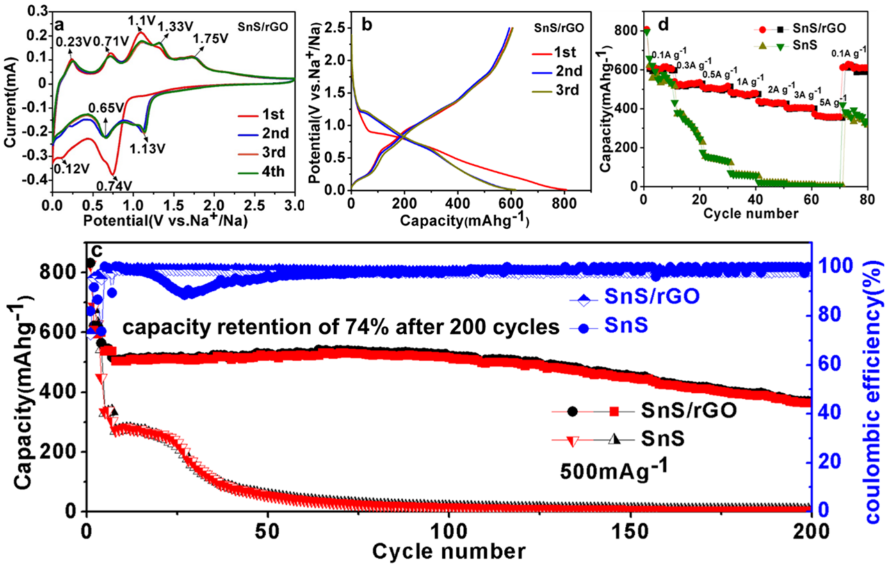

**Figure 4.** (a) CV curves of SnS/rGO at 0.1 mV $s^{-1}$; (b) galvanostatic discharge/charge curves of SnS/rGO for initial three cycles at 0.1 A $g^{-1}$; (c) cycling performance of SnS and SnS/rGO at 0.5 A $g^{-1}$; (d) rate performance of SnS/rGO and SnS at different current densities.

composite because of the release of $NH_3$ from L-cysteine.[43] The N spectrum in Figure 2b reveals it has three kinds of N species: pyridine N, pyrrole N, and oxidized N. The pyridine N and pyrrole N are ascribed to the N atoms substituting the C atoms of graphene on the edges or defect sites, which might increase the electrochemical activity sites for $Na^+$ intercalation/extraction.[43,49,50] The same results can be observed in C 1s of the SnS/rGO composite, Figure 2c. The primary carbon species is graphitic carbon, which is located at 284.6 eV. In addition, there are also other two weak peaks at 285 and 289 eV, implying the presence of C−N/C−S and O=C=O bonds. On comparison of S 2p spectra of SnS and SnS/rGO composites (Figure 2d), it shows that peaks at 162.35 and 161.2 eV can be assigned to the S $2p_{3/2}$ and S $2p_{1/2}$, respectively, of $S^{2-}$ in SnS. For the SnS/rGO composite, S $2p_{3/2}$ and S $2p_{1/2}$ peaks of SnS slightly shift to lower binding energy, demonstrating that the density of electron clouds around SnS increased after incorporation of graphene.[46] Other two peaks located at 165.07 and 163.8 eV are caused by the formation of −C−S−C− heterocyclic configuration during heat-treatment in SnS/rGO.[43,51] For the Sn 3d spectra of SnS and SnS/rGO composites (Figure 2e), there are two peaks at 494.1 and 485.7 eV, which are indexed to $Sn^{2+}$. Two small peaks at 494.1 and 486.8 eV are ascribed to $Sn^{4+}$, indicating edges of SnS were oxidized because of the unstable state of $Sn^{2+}$.[52,53] The peak intensity of $Sn^{4+}$ in SnS/rGO is much stronger than that of pure SnS, which may be ascribed to expose more edges for SnS/rGO because of smaller particle sizes. The high-resolution spectrum of Sn 3d in SnS/rGO reveals a little shift toward lower bond energy than those of pure SnS, which suggests possible shifting of electron clouds from graphene to SnS. This might be attributable to the fact that SnS has the characteristic of a p-type semiconductor and it has a large number of electron holes.[46]

Figure 3a is the scanning electron microscopy (SEM) of SnS, revealing thick nanosheet structures with aggregated and stacked bulk structures. The transmission electron microscopy (TEM) of Figure 3b displays that the individual SnS nanosheet has nanoparticles of size more than 200 nm. The HRTEM of SnS (Figures 3c and S1) reveals a thin amorphous layer on the surface of SnS nanosheets, probably due to the oxidation of SnS when exposed to air. Figure 3d shows the lattice fringes of about 0.283, 0.279, and 0.202 nm, which can be assigned to the (111), (040), and (141) planes of orthorhombic SnS, respectively. Figure 3e of SnS/rGO reveals that there are many SnS nanosheets tightly covered by the graphene framework and have a thickness of 10−30 nm without stacking and agglomeration (Figure 3f). Figure 3g,h exhibits three lattice fringes of 0.21, 0.279, and 0.171 nm, corresponding to the (210), (040), and (160) planes of SnS, respectively. Figure 3j depicts the line profiles of a curled edge as marked in Figure 3g, showing the (040) plane of orthorhombic SnS. The results verify that SnS nanosheets exposed many open edges along (*l*00) and (00*l*) directions under the confinement of graphene during the synthesis process, as illustrated in Figure 3i. From the SnS laminar structures from [100] and [001] axes (Figure 3k,l), those exposed edges can provide an easy way to facilitate $Na^+$ transfer into the (0*l*0) plane.

Figures 4a and S2a display the CV curves of SnS/rGO and SnS for the first four cycles. For the first cathodic scan of SnS/rGO, a significant reduction peak appeared at 0.74 V and disappeared at the subsequent cycles, which is attributable to the formation of the SEI layer. In addition, the ex situ XRD results (Figure S3) show that when discharged to 0.74V, the main SnS peaks do not exist, while Sn and $Na_2S$ peaks appear. This indicates that this initial discharge process is the conversion reaction of SnS to Sn and $Na_2S$ ($SnS + 2Na^+ + 2e = Na_2S$), which is in agreement with the previous report.[18] Then, when discharged to 0.01 V, other cathodic peaks were located at 0.12 V and below 0.02 V. Combing with the XRD results, it reflects that the conversion of Sn to $Na_xSn$ is a multistep reaction of Sn. In the first anodic scan of SnS/rGO, there are two small peaks located at 0.23 and 0.71 V, which are considered as dealloying of $Na_xSn$. Then, a strong peak appears at 1.1 V, and it is mainly composed of Sn and $Na_xS$ at this stage, corresponding to the beginning of conversion from Sn to SnS. When charged to 2.5 V, the peaks of SnS can be observed again, which means the reversible redox process of SnS/rGO. However, there is no $Na_xSn$ alloy found in the first charge/discharge process in the ex-situ XRD results, which makes it

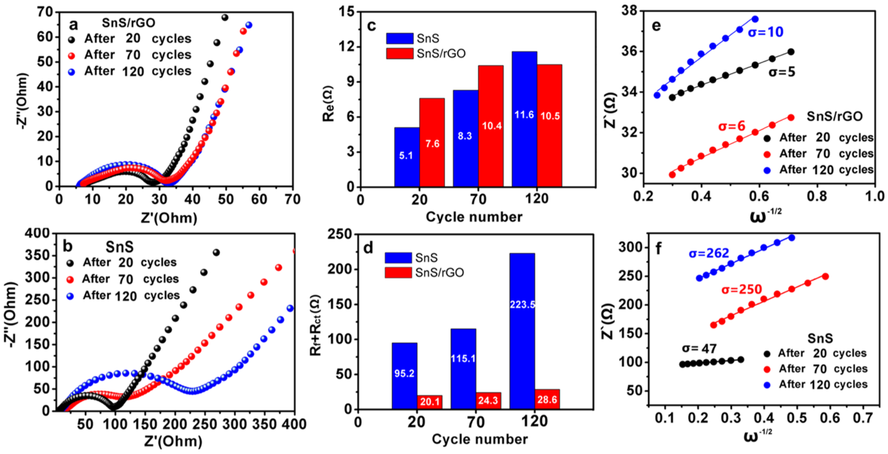

**Figure 5.** Nyquist plots of (a) SnS/rGO and (b) SnS after different cycles (c) $R_e$ of SnS/rGO and SnS after different cycles; (d) $R_f + R_{ct}$ of SnS/rGO and SnS after different cycle; (e,f) resistance of $Z'$ vs $\omega^{-1/2}$ after different cycle for SnS/rGO and SnS.

probable that formation of $Na_xSn$ alloy is amorphous. From the second cycle to the fourth cycle, a pair of reduction/oxidation peaks located at 1.13 V/1.33 V are related to the mutually redox reaction of SnS and Sn, which indicates that the conversion reaction between SnS and Sn is reversible.[46,54] In addition, the peaks of 0.23 V/0.12 V and 0.71 V/0.65 V can be assigned to further sodium−tin conversion reactions.[27] Note that a significant oxidation peak appears at 1.75 V and does not disappear in the following cycles. This can be related to the desodiation reaction of $Na_2S_x$ from the −C−S−C bond of graphene.[43] There is no further S-oxidation reaction observed at a higher voltage, indicating that S is stable.[50] Oxidation/reduction peaks of SnS/rGO in second to fourth cycles are highly overlapped, suggesting good electrochemical stability.

Figure 4b displays the charge/discharge profiles of SnS/rGO for the first three cycles. The first discharge/charge capacities of SnS/rGO are 807 and 603 mA h g$^{-1}$, with an initial Coulombic efficiency of 74%. The large irreversible capacity is mainly ascribed to the consumption of Na$^+$ to form SEI films in the initial cycle. This result is also in agreement with the CV curve of SnS/rGO. It also maintains a discharge capacity of 575 mA h g$^{-1}$ after 100 cycles with still 95% capacity retention at 100 mA g$^{-1}$ (Figure S2b), while the SnS slowly decreases from 660 to 110 mA h g$^{-1}$. Even at a high current density of 500 mA g$^{-1}$ (Figure 4c), the SnS/rGO composite can still maintain capacity of 500 mA h g$^{-1}$/370 mA h g$^{-1}$ after 100/200 cycles, which is comparable with other published works related to SnS-based anode materials (Table S3). Figure S2c,d show some charge/discharge curves of SnS/rGO and SnS. The polarization of SnS/rGO is obviously smaller than that of SnS at every current densities, revealing that the graphene conductive framework provides a more efficient electron pathway, resulting in an increased capability of Na$^+$ ion sodiation/desodiation. We also further tested the electrochemical properties of SnS/rGO at higher loading mass (2.3 ± 0.1 mg cm$^{-2}$ for each Φ14 electrode piece) to consider the influence of loading mass for half SIB (labeled as SnS/rGO-2.3mg/cm$^2$). The electrochemical properties are exhibited in the Figure S4. When the active material is increased twice, SnS/rGO-2.3mg/cm$^2$ exhibits initial discharge/charge capacities of 574/454 mA h g$^{-1}$ with Coulombic efficiency of 79%. There is only slight decrease in the discharge/charge capacity compared with the specific capacity of the SnS/rGO electrode of lower mass loading. Besides, the rate performance of SnS/rGO-2.3mg/cm$^2$ also displays improved reversible capacity at 2, 3, and 5 A g$^{-1}$, indicating that Na$^+$ redox kinetics for SnS/rGO at higher electrode thickness is still remained. In stark contrast, the capacity of pure SnS rapidly decreases to almost zero after 70 cycles. Figure S5 shows the charge/discharge profiles of the SnS after 20, 50, and 70 cycles, which shows that the polarization sharply increases. The excellent cycling performance of SnS/rGO is attributed to the smaller SnS nanosheets whose confined growth by rGO compared to pure SnS. It largely increases sodium ion diffusion kinetics from the open edge of SnS layers, which increases its capacity at high current density. Figure 4d shows that the SnS/rGO composite delivered reversible capacities of 605, 520, 500, 477, 430, 400, and 360 mA h g$^{-1}$ at 0.1, 0.3, 0.5, 1, 2, 3, and 5 A g$^{-1}$, respectively. It can be quickly restored to a capacity of 610 mA h g$^{-1}$ after going back to 100 mA g$^{-1}$, indicating the satisfied electrochemical stability of SnS/rGO. However, the capacity of pure SnS decreased dramatically from 0.3 to 1 A g$^{-1}$ and almost all capacity was lost at higher current densities.

EIS analyses of SnS and SnS/rGO after 20th, 70th, and 120th cycles show that both the Nyquist plots of SnS/rGO and SnS compose of one semicircle along with a straight line (Figure 5a,b). The equivalent circuit, as illustrated in Figure S6, contains the electrolyte resistance ($R_e$), combination of the surface SEI film and charge transfer resistance ($R_f + R_{ct}$), CPE, and Warburg impedance ($W_o$).[55] Both SnS and SnS/rGO have similar $R_e$ (Figure 5c), indicating there is no big difference in electrolyte resistance. However, the surface film resistance and charge transfer resistance (Figure 5d) for SnS dramatically increased as cycling performance increased (95.2, 115.1, 223.5 Ω at 20th, 70th, and 120th), compared with the much smaller change after different cycles for SnS/rGO electrode (20.1, 24.3, and 28.6 Ω at 20th, 70th, and 120th), which shows that SnS/rGO has higher electronic conductivity and ionic conductivity than SnS.

At the same time, Na$^+$ diffusion coefficient are calculated by the low frequency range of EIS according to the following formula[56,57]

$$D_{Na^+} = \frac{R^2T^2}{2A^2n^4F^4C^2\sigma^2} \tag{3}$$

where $R$ represents the gas constant; $A$ is the surface area of the electrode; $T$ is the reaction temperature; $F$ is Faraday constant; n is the number of electrons involved in reaction; and

DOI: 10.1021/acsami.9b14098
ACS Appl. Mater. Interfaces 2019, 11, 41363−41373

$C$ is the concentration of $Na^+$ in the electrode material. $\sigma$ is the Warburg factor, which can be obtained directly from the linear fitting slope according to resistance of $Z'$ versus $\omega^{-1/2}$ (Figure 5e,f). Table 1 shows the $Na^+$ diffusion coefficient of SnS and SnS/rGO after different cycles. It can be seen that the $Na^+$ diffusion coefficient of SnS decreases sharply as the number of cycles increases ($6.22 \times 10^{-15}$, $2.19 \times 10^{-16}$, and $1.99 \times 10^{-16}$ $cm^2\ s^{-1}$ at 20th, 70th, and 120th, respectively), which is lower about 100 to 1000 times after different cycles for the SnS/rGO electrode ($4.78 \times 10^{-13}$, $3.07 \times 10^{-13}$, and $1.37 \times 10^{-13}$ $cm^2\ s^{-1}$ at 20th, 70th, and 120th, respectively), which means that SnS/rGO has higher $Na^+$ diffusion kinetics than SnS. SEM images after 70 cycles of SnS (Figure S7a) and SnS/rGO (Figure S7b) show that SnS/rGO remains as nanosheet structures in the matrix of the electrode without agglomeration, while SnS displays different shapes compared with original layered structures. TEM of SnS after 70 cycles (Figure S7c) also indicates that the layered structures of original SnS are cracked and form random morphology, demonstrating a large volume change during cycling. In contrast, SnS/rGO (Figure S7d) presents smaller nanosheets dispersed in the rGO framework. It confirms that rGO can inhibit the structural transformation of SnS to some extent and promotes the formation of a stable interface structure to maintain the integrity of the electrode structure.

**Table 1. Comparison of $D_{Na^+}$ (Na Ion Diffusion Coefficient) between SnS and SnS/rGO after Different Cycles**

| $D_{Na}$ ($cm^2\ s^{-1}$) | after 20 cycles | after 70 cycles | after 120 cycles |
|---|---|---|---|
| SnS | $6.22 \times 10^{-15}$ | $2.19 \times 10^{-16}$ | $1.99 \times 10^{-16}$ |
| SnS/rGO | $4.78 \times 10^{-13}$ | $3.07 \times 10^{-13}$ | $1.37 \times 10^{-13}$ |

Figure 6a,b showed the CV curves of SnS/rGO and SnS from 0.1 to 7 mV $s^{-1}$, respectively. With increase of the scanning rate, the conversion peak of SnS (~1 V for cathodic process and 1.4 V for anodic process) obviously decreases compared with that of SnS/rGO, which indicates that the $Na^+$ intercalation in the SnS layers is gradually inhibited.

The impacts of diffusion and capacitance on the charge/discharge process are analyzed using the following formula.[43]

$$i = av^b \tag{4}$$

$$i(v) = k_1 v + k_2 v^{1/2} \tag{5}$$

where $a$ and $b$ are adjustable parameters, $i$ and $v$ are the peak current and scan rate.

According to the previous reports, the value of $b$ is used to measure the pattern of charging and discharging behaviors: $b = 0.5$ means the capacity is controlled by the diffusion pattern, while $b = 1.0$ reflects capacity as the capacitance controlled pattern. The b value of the cathodic and anodic scan for SnS/rGO are calculated to be 0.939 and 0.886, respectively, (Figure 6c), indicating dominant pseudocapacitance contribution at a high sweep rate. In contrast, the $b$ value for SnS is 0.652 and 0.614 (Figure 6d), which means the diffusion-controlled $Na^+$ storage is the main contribution for whole reversible capacity. The result is also supported by the previous reports of SnS/rGO materials for sodium-ion batteries.[43,46,58]

The total current response ($i(v)$) consists of the diffusion-controlled process ($k_2 v^{1/2}$) and the capacitive-controlled process ($k_1 v$) at the corresponding voltage. Figures 6e and S8a show the area proportions of the diffusion contribution and capacitance contribution of SnS/rGO and SnS in the CV curve at a scan rate of 7 mV $s^{-1}$, respectively, which directly reflect the main capacity contribution coming from $Na^+$ pseudocapacitance storage at a high scan rate. Figures 6f and S8b further show the calculated capacitive contribution rate of SnS/rGO and SnS, which can be seen that it occupies high capacitive contribution rate at every sweep rate for SnS/rGO. The phenomenon implies that $Na^+$ storage mechanism in the SnS/rGO composite are mainly ascribed to the rapid chemical adsorption/desorption because of the abundant edges of layered SnS and rGO. However, it is noteworthy that the pseudocapacitance contributions of SnS at different sweep rates are very low. At 0.1 mV $s^{-1}$, the pseudocapacitance contribution of SnS is only 22%. Even at 7 mV $s^{-1}$, the pseudocapacitance contribution ratio is 67%. As a result, the diffusion-controlled $Na^+$ storage in pure SnS might be largely hinderedbecause of the larger bulk size of pure SnS, which further causes low rate capability.

Based on the above analysis results, introduction of graphene in the SnS structure first decreases the agglomeration of SnS

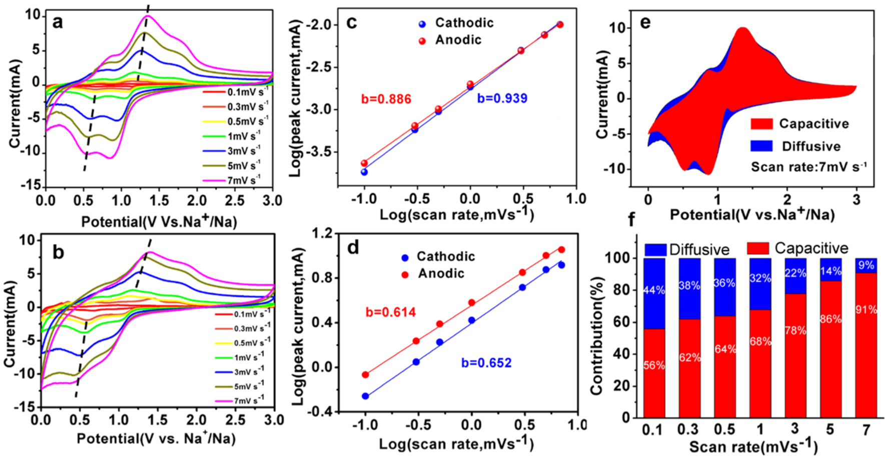

**Figure 6.** CV curves of (a) SnS/rGO and (b) SnS anodes in SIB at different scan rates; (c,d) are the $b$ values fitted by log $i$ and log $v$ of SnS/rGO and SnS, respectively; (e) capacitive and diffusive contributions of SnS/rGO at 7 mV $s^{-1}$; and (f) the percentage of SnS/rGO capacitive contribution from 0.1 to 7 mV $s^{-1}$.

DOI: 10.1021/acsami.9b14098
ACS Appl. Mater. Interfaces 2019, 11, 41363−41373

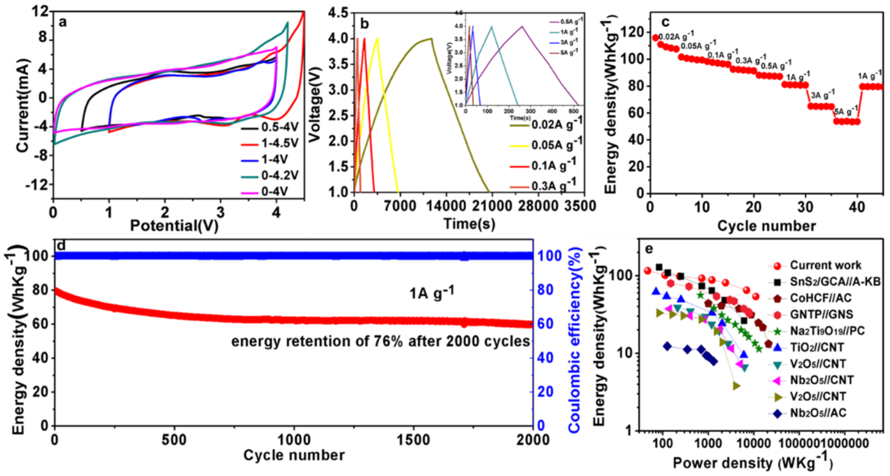

**Figure 7.** (a) CV curve of AC//SnS/rGO SICs at different potential windows at 0.1 mV $s^{-1}$; (b) time−voltage profiles of the AC//SnS/rGO SIC device from 0.02 to 5 A $g^{-1}$; (c) rate performance of the AC//SnS/rGO SIC device at different current densities; (d) long-term cycling stability of the AC//SnS/rGO SIC device at 1 A $g^{-1}$ (e) Ragone plots of SICs in the current work compared with that reported in previous studies.

during the fabrication process. Because of the confinement of graphene, the growth of SnS along (0*l*0) and (00*l*) directions is suppressed, which displays smaller thickness and particle size. Second, the smaller SnS nanosheets exposed many open edges along (*l*00) and (00*l*) directions, providing an easy way to facilitate $Na^+$ transfer into the (0*l*0) plane, which can be confirmed by the $Na^+$ diffusion coefficients after different cycles. In addition, these active open edges also possess a lot of vacancies because of the presence of $Sn^{4+}$−O, which provide many active sites for $Na^+$ pseudocapacitance storage on the surface of SnS. Meanwhile, the presence of pyridine N, pyrrole N, and C−N/C−S on the edges or defect sites in the graphene structure also synergistically increases electrochemical activity sites for $Na^+$ storage.

Figure 7a shows the CV curves of AC//SnS/rGO SICs at different potential windows with 0.1 mV $s^{-1}$. It can be clearly seen that no matter the voltage window 0−4.2 or 1−4.5 V, the CV curves of the AC//SnS/rGO SICs display large polarization above 4.2 V, which cannot display an ideal rectangular shape. When the potential window was set at 0−4, 0.5−4, and 1−4 V, there is only a minor polarization near the 4 V. In order to find the optimal potential window, we further compare the cycle stability of AC//SnS/rGO SICs at the voltage window at 0−4, 0.5−4, and 1−4 V at 1 A $g^{-1}$, respectively.

When adjusting the voltage window at 1−4 V, the overall performance is better than those of other voltage window ranges of 0−4 and 0.5−4 V, which indicates that the voltage window has reached an optimal match for this SIC system. This might be result from at the lower working voltage, partial irreversible Na−Sn alloying reaction may occur due to the unbalance cathode/anode reaction rate. Therefore, we consider 1−4 V as the optimized voltage window to test the performance of AC//SnS/rGO SICs. The electrochemical performance and energy density of AC//SnS/rGO SICs with a different mass ratio of AC to SnS/rGO were evaluated during 1−4 V, and the results are shown in Figure S10a. First, the electrochemical properties of the AC half-cell are tested to choose the appropriate cathode/anode ratio. As shown in Figure S9, the active carbon displays specific capacities of 100, 71, 62, 53, 50, 48, 40, and 33 mA h $g^{-1}$ at 0.02, 0.05, 0.1, 0.3, 0.5, 1, 2, and 3 A $g^{-1}$, respectively. Besides, it obtains stable specific capacity of 45 mA h $g^{-1}$ at 0.5 A $g^{-1}$, which is suitable as the cathode material for SICs. The test results of active substances with different mass ratios of cathode and anode electrodes are shown in Figure S10b,c. When the ratio of cathode- and anode-active substances was set at 2:1 (the cathode and anode active substances was 2.2 ± 0.1 mg $cm^{-2}$ and 1.1 ± 0.1 mg $cm^{-2}$ for each Φ14 electrode piece, respectively), the rate and long-term cycle performance were the best, which indicates the balance of capacity of cathode/anode and the maximum energy density of the SIC device.[59,60] Hence, the optimal cathode and anode mass ratio was to be 2:1 for the AC//SnS/rGO SICs device. The time−voltage profiles of AC//SnS/rGO SICs (Figure 7b) display linear relationship from 0.02 to 5 A $g^{-1}$, implying capacitance characteristic during the charge/discharge process. The rate performance of the AC//SnS/rGO SIC device is shown in Figure 7c with energy densities of 115, 101, 98, 92, 88, 81, 65, and 53 W h $kg^{-1}$ at 0.02, 0.05, 0.1, 0.3, 0.5, 1, 3, and 5 A $g^{-1}$, respectively. When the current density returns to 1 A $g^{-1}$, the AC//SnS/rGO SIC device can be quickly restored to the energy density of 80 W h $kg^{-1}$. The energy density of AC//SnS/rGO SICs is 61 W h $kg^{-1}$ with high energy maintain, which can be achieve 76% after 2000 cycles at 1 A $g^{-1}$ (Figure 7d). As we have mentioned in the introduction, the anode materials for the sodium-ion hybrid capacitor are needed to have high electrochemical reaction kinetics to match the rapid adsorption/desorption non-Faraday reaction process of cathode materials. The main $Na^+$ storage mechanism in anode materials is reliable on $Na^+$ intercalation/extraction from the material crystal structure, which is always hindered by the sluggish $Na^+$ transfer and insufficient $Na^+$ redox kinetics. Hence, it is not suitable to use the diffusion-controlled anode materials in the system of SICs. In addition, the diffusion-controlled anode materials also suffer from repeated crystal structural changes, which might result in the collapse of the structure. From this view, it is also inappropriate to use these materials for long span of SICs. From this work, we find that although SnS is an $Na^+$ intercalation mechanism anode material, according to introduction of graphene, the growth of SnS along (0*l*0) and (00*l*) directions is suppressed, which displays smaller thickness and particle size. Meanwhile, the active open edges also possess a lot of vacancies, which provide many active sites for $Na^+$ pseudocapacitance storage on the surface of SnS. Furthermore, the presence of pyridine N, pyrrole N, and C−N/C−S on the edges or defect sites in the graphene structure also synergistically increases electrochemical activity sites for $Na^+$ pseudocapacitance storage. As a result, the predominance function of $Na^+$ pseudocapacitance storage for the SnS/rGO composite makes it suitable to balance the difference of $Na^+$ back and forth in the cathode/anode materials in SICs. The Ragone plot of AC//SnS/rGO SICs in Figure 7e was compared with SIC data reported in literature and showed AC//SnS/rGO SICs delivered a high energy density of 113 W h $kg^{-1}$ under power density of 101 W $kg^{-1}$. The power density and energy density of the AC//SnS/rGO SICs are superior to several SIC devices previously reported, such as $SnS_2$/GCA//A-KB,[37] CoHCF//AC,[33] GNTP//GNS,[61] $Na_2Ti_9O_{19}$//PC,[62] $TiO_2$//CNT,[63] $V_2O_5$//CNT,[64] $Nb_2O_5$//CNT,[65] $V_2O_5$//CNT,[66] and $Nb_2O_5$//AC[67] devices.

The higher cycling stability for SnS/rGO as the SIC anode than as the anode for SIBs can be analyzed by the following reasons. First, the presodiation SnS/rGO electrode as the anode can avoid large irreversible $Na^+$ loss at the initial stage. In addition, compared with the SnS/rGO electrode for the SIC, it might also suffer from some side reactions from the sodium metal during the repeated cycling for SIBs, such as sodium dendritic growth at low voltage potential, which results in capacity decaying of SnS/rGO after long cycling. The optimize voltage window for the AC//SnS/rGO hybrid capacitor (1−4 V) probably suppresses those side reaction. The high energy density of AC//SnS/rGO SICs might be resulted from fast uptaking and releasing of sodium ions to and from SnS nanosheets. In addition, the diffusion of $Na^+$ ions along the (00*l*) direction is more accessible to (0*l*0) direction for those 2D layered materials. DFT calculation[68] indicated that $Sn^{2+}$ at layer edges is not stable. It inclines to covert to $Sn^{4+}$ through oxidation, which means it possesses abundant vacancies to strength $Na^+$ storage on its edges. Besides, S and N codoped in graphene would also promote $Na^+$ surface adsorption/desorption. As a result, the SnS/rGO electrode for the SIC can maintain higher electrochemical stability.

## 4. CONCLUSIONS

SnS nanosheets confined growth by S and N codoped graphene were synthesized through hydrothermal growth of $SnS_2$ in combination with in situ electrostatic self-assembly followed by annealing. Smaller SnS nanosheets tightly covered by graphene possess open edges with abundant active sites to facilitate sodium ion adsorption and shorten diffusion pathways, resulting in high sodium ion storage capacity and excellent transport kinetics. The SICs with SnS/rGO as the anode and AC as the cathode delivered 80 W h $kg^{-1}$ with a retention of 76% for 2000 cycles at 1 A $g^{-1}$, and 54 W h $kg^{-1}$ with a power density of 11 100 W $kg^{-1}$.

## ■ ASSOCIATED CONTENT

### Ⓢ Supporting Information

The Supporting Information is available free of charge on the ACS Publications website at DOI: 10.1021/acsami.9b14098.

XRD, zeta potentials values, analysis of SnS/rGO and SnS crystalline size, SEM, CV, and GCD curves (PDF)

## ■ AUTHOR INFORMATION

### Corresponding Authors

*E-mail: wangmingshan@swpu.edu.cn (M.W.).
*E-mail: lixing@swpu.edu.cn (X.L.).
*E-mail: gzcao@u.washington.edu (G.C.).

### ORCID

Mingshan Wang: 0000-0001-5461-3951
Guozhong Cao: 0000-0001-6539-0490

### Notes

The authors declare no competing financial interest.

## ■ ACKNOWLEDGMENTS

We acknowledge the National Natural Science Foundation of China (grant nos. 51604250, 51502250, 51474196), the Science & Technology Department of Sichuan Province (grant nos. 2019YFG0220, 2016RZ0071, 2017JQ0044), Youth Science and Technology Innovation Team of Energy Material Electrochemistry of Southwest Petroleum University (grant no. 2015CXTD04), and the China Scholarship Council (no. 201708515143) for their financial support.

## ■ REFERENCES

(1) Armand, M.; Tarascon, J.-M. Building Better Batteries. *Nature* **2008**, *451*, 652.

(2) Motavalli, J. Technology: A solid future. *Nature* **2015**, *526*, S96.

(3) Van Noorden, R. The Rechargeable Revolution: a Better Battery. *Nat.News* **2014**, *507*, 26.

(4) Chao, D.; Ouyang, B.; Liang, P.; Huong, T. T. T.; Jia, G.; Huang, H.; Xia, X.; Rawat, R. S.; Fan, H. J. C-Plasma of Hierarchical Graphene Survives SnS Bundles for Ultrastable and High Volumetric Na-Ion Storage. *Adv. Mater.* **2018**, *30*, 1804833.

(5) Xie, X.; Ao, Z.; Su, D.; Zhang, J.; Wang, G. $MoS_2$/graphene Composite Anodes with Enhanced Performance for Sodium-ion Batteries: the Role of the Two-dimensional Heterointerface. *Adv. Funct. Mater.* **2015**, *25*, 1393−1403.

(6) Wang, Y.; Zhang, Y.; Shi, J.; Pan, A.; Jiang, F.; Liang, S.; Cao, G. S-doped Porous Carbon Confined SnS Nanospheres with Enhanced Electrochemical Performance for Sodium-ion Batteries. *J. Mater. Chem. A* **2018**, *6*, 18286−18292.

(7) Xue, P.; Wang, N.; Wang, Y.; Zhang, Y.; Liu, Y.; Tang, B.; Bai, Z.; Dou, S. Nanoconfined SnS in 3D Interconnected Macroporous Carbon as Durable Anodes for Lithium/sodium Ion Batteries. *Carbon* **2018**, *134*, 222−231.

(8) Wang, Z.-Q.; Wang, M.-S.; Yang, Z.-L.; Bai, Y.-S.; Ma, Y.; Wang, G.-L.; Huang, Y.; Li, X. $SnO_2$ /Sn Nanoparticles Embedded in an Ordered, Porous Carbon Framework for High-Performance Lithium-Ion Battery Anodes. *ChemElectroChem* **2017**, *4*, 345−352.

(9) Dong, S.; Li, C.; Li, Z.; Zhang, L.; Yin, L. Mesoporous Hollow Sb/ZnS@C Core-Shell Heterostructures as Anodes for High-Performance Sodium-Ion Batteries. *Small* **2018**, *14*, 1704517.

(10) Tu, F.; Xu, X.; Wang, P.; Si, L.; Zhou, X.; Bao, J. A Few-Layer $SnS_2$/Reduced Graphene Oxide Sandwich Hybrid for Efficient Sodium Storage. *J. Phys. Chem. C* **2017**, *121*, 3261−3269.

(11) Hwang, J.-Y.; Myung, S.-T.; Sun, Y.-K. Sodium-ion Batteries: Present and Future. *Chem.Soc. Rev.* **2017**, *46*, 3529−3614.

(12) Lu, Y. C.; Ma, C.; Alvarado, J.; Dimov, N.; Meng, Y. S.; Okada, S. Improved Electrochemical Performance of Tin-sulfide Anodes for Sodium-ion Batteries. *J. Mater. Chem. A* **2015**, 3, 16971−16977.

(13) Zhou, L.; Zhang, K.; Sheng, J.; An, Q.; Tao, Z.; Kang, Y.-M.; Chen, J.; Mai, L. Structural and Chemical Synergistic Effect of CoS Nanoparticles and Porous Carbon Nanorods for High-performance Sodium Storage. *Nano Energy* **2017**, *35*, 281−289.

(14) Liu, Z.; Lu, T.; Song, T.; Yu, X.-Y.; Lou, X. W.; Paik, U. Structure-designed synthesis of $FeS_2$@C yolk-shell nanoboxes as a high-performance anode for sodium-ion batteries. *Energy Environ. Sci.* **2017**, *10*, 1576−1580.

(15) Su, D.; Dou, S.; Wang, G. Ultrathin $MoS_2$ Nanosheets as Anode Materials for Sodium-Ion Batteries with Superior Performance. *Adv. Energy Mater.* **2015**, *5*, 1401205.

(16) Rao, C. N. R.; Ramakrishna Matte, H. S. S.; Maitra, U. Graphene Analogues of Inorganic Layered Materials. *Angew. Chem., Int. Ed.* **2013**, *52*, 13162−13185.

(17) Xia, C.; Zhang, F.; Liang, H.; Alshareef, H. N. Layered SnS Sodium Ion Battery Anodes Synthesized Near Room Temperature. *Nano Res.* **2017**, *10*, 4368−4377.

(18) Wu, L.; Lu, H.; Xiao, L.; Qian, J.; Ai, X.; Yang, H.; Cao, Y. A tin(ii) sulfide-carbon anode material based on combined conversion and alloying reactions for sodium-ion batteries. *J. Mater. Chem. A.* **2014**, *2*, 16424−16428.

(19) Ma, C.; Xu, J.; Alvarado, J.; Qu, B.; Somerville, J.; Lee, J. Y.; Meng, Y. S. Investigating the Energy Storage Mechanism of $SnS_2$-rGO Composite Anode for Advanced Na-ion Batteries. *Chem. Mater.* **2015**, *27*, 5633−5640.

(20) Liu, Y.; Yu, X.-Y.; Fang, Y.; Zhu, X.; Bao, J.; Zhou, X.; Lou, X. W. Confining $SnS_2$ Ultrathin Nanosheets in Hollow Carbon Nanostructures for Efficient Capacitive Sodium Storage. *Joule* **2018**, *2*, 725−735.

(21) Fei, L.; Xu, M.; Jiang, J.; Ng, S. M.; Shu, L.; Sun, L.; Xie, K.; Huang, H.; Leung, C. W.; Mak, C. L.; Wang, Y. Three-dimensional Macroporous Graphene Monoliths with Entrapped $MoS_2$ Nanoflakes From Single-step Synthesis for High-performance Sodium-ion Batteries. *RSC Adv.* **2018**, *8*, 2477−2484.

(22) Hu, X.; Chen, J.; Zeng, G.; Jia, J.; Cai, P.; Chai, G.; Wen, Z. Robust 3D Macroporous Structures with SnS Nanoparticles Decorating Nitrogen-doped Carbon Nanosheet Networks for High Performance Sodium-ion Batteries. *J. Mater. Chem. A.* **2017**, *5*, 23460−23470.

(23) Choi, S. H.; Kang, Y. C. Synergetic Effect of Yolk-shell Structure and Uniform Mixing of SnS-$MoS_2$ Nanocrystals for Improved Na-ion Storage Capabilities. *ACS Appl. Mater. Interfaces* **2015**, *7*, 24694−24702.

(24) Dong, S.; Li, C.; Li, Z.; Zhang, L.; Yin, L. Mesoporous Hollow Sb/ZnS@C Core-shell Heterostructures as Anodes for High-performance Sodium-ion Batteries. *Small* **2018**, *14*, 1704517.

(25) Liu, C.; Neale, Z.; Zheng, J.; Jia, X.; Huang, J.; Yan, M.; Tian, M.; Wang, M.; Yang, J.; Cao, G. Expanded Hydrated Vanadate for High-performance Aqueous Zinc-ion Batteries. *Energy Environ. Sci.* **2019**, *12*, 2273−2285.

(26) Pan, Q.; Xie, J.; Zhu, T.; Cao, G.; Zhao, X.; Zhang, S. Reduced Graphene Oxide-induced Recrystallization of NiS Nanorods to Nanosheets and The Improved Na-storage Properties. *InCh* **2014**, *53*, 3511−3518.

(27) Zhu, C.; Kopold, P.; Li, W.; van Aken, P. A.; Maier, J.; Yu, Y. A General Strategy to Fabricate Carbon-coated 3D Porous Interconnected Metal Sulfides: Case Study of SnS/C Nanocomposite for High-performance Lithium and Sodium ion batteries. *Adv. Sci.* **2015**, *2*, 1500200.

(28) Wang, Q.; Ge, X.; Xu, J.; Du, Y.; Zhao, X.; Si, L.; Zhou, X. Fabrication of Microporous Sulfur-doped Carbon Microtubes for High-performance Sodium-ion Batteries. *ACS Appl. Energy Mater.* **2018**, *1*, 6638−6645.

(29) Zou, G.; Wang, C.; Hou, H.; Wang, C.; Qiu, X.; Ji, X. Controllable Interlayer Spacing of Sulfur-doped Graphitic Carbon Nanosheets for Fast Sodium-ion Batteries. *Small* **2017**, *13*, 1700762.

(30) Li, H.; Lang, J.; Lei, S.; Chen, J.; Wang, K.; Liu, L.; Zhang, T.; Liu, W.; Yan, X. A High-Performance Sodium-ion Hybrid Capacitor Constructed by Metal-organic Framework-derived Anode and Cathode Materials. *Adv. Funct. Mater.* **2018**, *28*, 1800757.

(31) Jian, Z.; Raju, V.; Li, Z.; Xing, Z.; Hu, Y.-S.; Ji, X. A High-power Symmetric Na-ion Pseudocapacitor. *Adv. Funct. Mater.* **2015**, *25*, 5778−5785.

(32) Zhao, Y.; Zhang, W.-B.; Zhao, Z.-Y.; Li, K.; Wang, Y.-K.; Li, Y.; Kong, L.-B. Synthesis and Evaluation of Three-dimensional Nickel Molybdate Nano-sheets on Nickel Foam as Self-Supported Electrodes for Sodium-ion Hybrid Capacitors. *Mater. Res. Express* **2018**, *5*, 065525.

(33) Wang, J.-G.; Zhang, Z.; Zhang, X.; Yin, X.; Li, X.; Liu, X.; Kang, F.; Wei, B. Cation Exchange Formation of Prussian Blue Analogue Submicroboxes for High-performance Na-ion Hybrid Supercapacitors. *Nano Energy* **2017**, *39*, 647−653.

(34) Chen, N.; Han, C.; Shi, R.; Xu, L.; Li, H.; Liu, Y.; Li, J.; Li, B. Carbon Coated $MoS_2$ Nanosheets Vertically Grown on Carbon Cloth as Efficient Anode for High-performance Sodium Ion Hybrid Capacitors. *Electrochim. Acta* **2018**, *283*, 36−44.

(35) Wang, H.; Zhu, C.; Chao, D.; Yan, Q.; Fan, H. J. Nonaqueous Hybrid Lithium-Ion and Sodium-Ion Capacitors. *Adv. Mater.* **2017**, *29*, 1702093.

(36) Wang, J.; Dong, S.; Ding, B.; Wang, Y.; Hao, X.; Dou, H.; Xia, Y.; Zhang, X. Pseudocapacitive Materials for Electrochemical Capacitors: From Rational Synthesis to Capacitance Optimization. *Nat. Sci. Rev.* **2016**, *4*, 71−90.

(37) Cui, J.; Yao, S.; Lu, Z.; Huang, J.-Q.; Chong, W. G.; Ciucci, F.; Kim, J.-K. Revealing Pseudocapacitive Mechanisms of Metal Dichalcogenide $SnS_2$/graphene-CNT Aerogels for High-Energy Na Hybrid Capacitors. *Adv. Energy Mater.* **2018**, *8*, 1702488.

(38) Zhang, Y.; Zhu, P.; Huang, L.; Xie, J.; Zhang, S.; Cao, G.; Zhao, X. Few-layered $SnS_2$ on Few-layered Reduced Graphene Oxide as Na-ion Battery Anode with Ultralong Cycle Life and Superior Rate Capability. *Adv. Funct. Mater.* **2015**, *25*, 481−489.

(39) Jiang, Y.; Wei, M.; Feng, J.; Ma, Y.; Xiong, S. Enhancing the Cycling Stability of Na-ion Batteries by Bonding $SnS_2$ Ultrafine Nanocrystals on Amino-functionalized Graphene Hybrid Nanosheets. *Energy Environ. Sci.* **2016**, *9*, 1430−1438.

(40) Le, Z.; Liu, F.; Nie, P.; Li, X.; Liu, X.; Bian, Z.; Chen, G.; Wu, H. B.; Lu, Y. Pseudocapacitive Sodium Storage in Mesoporous Single-crystal-like $TiO_2$-graphene Nanocomposite Enables High-Performance Sodium-ion Capacitors. *ACS Nano* **2017**, *11*, 2952−2960.

(41) Xiong, X.; Yang, C.; Wang, G.; Lin, Y.; Ou, X.; Wang, J.-H.; Zhao, B.; Liu, M.; Lin, Z.; Huang, K. SnS nanoparticles electrostatically anchored on three-dimensional N-doped graphene as an active and durable anode for sodium-ion batteries. *Energy Environ. Sci.* **2017**, *10*, 1757−1763.

(42) Wang, S.; Wang, X.; Jiang, S. P. Self-assembly of Mixed Pt and Au Nanoparticles on PDDA-functionalized Graphene as Effective Electrocatalysts for Formic Acid Oxidation of Fuel Cells. *Phys. Chem. Chem. Phys.* **2011**, *13*, 6883−6891.

(43) Sheng, J.; Yang, L.; Zhu, Y.-E.; Li, F.; Zhang, Y.; Zhou, Z. Oriented SnS Nanoflakes Bound on S-doped N-rich Carbon Nanosheets with a Rapid Pseudocapacitive Response as High-rate Anodes for Sodium-ion Batteries. *J. Mater. Chem. A* **2017**, *5*, 19745−19751.

(44) Biacchi, A. J.; Vaughn, D. D.; Schaak, R. E. Synthesis and Crystallographic Analysis of Shape-controlled SnS Nanocrystal Photocatalysts: Evidence for a Pseudotetragonal Structural Modification. *J. Am. Chem. Soc.* **2013**, *135*, 11634−11644.

(45) Wang, M.-S.; Wang, Z.-Q.; Yang, Z.-L.; Huang, Y.; Zheng, J.; Li, X. Carbon nanotube-graphene nanosheet conductive framework supported $SnO_2$ aerogel as a high performance anode for lithium ion battery. *Electrochim. Acta* **2017**, *240*, 7−15.

(46) Zhao, J.; Wang, G.; Hu, R.; Zhu, K.; Cheng, K.; Ye, K.; Cao, D.; Fan, Z. Ultrasmall-sized SnS nanosheets vertically aligned on carbon microtubes for sodium-ion capacitors with high energy density. *J. Mater. Chem. A* **2019**, *7*, 4047−4054.

(47) Wang, M.-S.; Wang, Z.-Q.; Jia, R.; Yang, Z.-L.; Yang, Y.; Zhu, F.-Y.; Huang, Y.; Li, X. Nano Tin Dioxide Anchored onto Carbon Nanotube/graphene Skeleton as Anode Material with Superior Lithium-ion Storage Capability. *J. Electroanal. Chem.* **2018**, *815*, 30−39.

(48) Wang, M.-S.; Wang, Z.-Q.; Jia, R.; Yang, Y.; Zhu, F.-Y.; Yang, Z.-L.; Huang, Y.; Li, X.; Xu, W. Facile Electrostatic Self-assembly of Silicon/reduced Graphene Oxide Porous Composite by Silica Assist as High Performance Anode for Li-ion Battery. *Appl. Surf. Sci.* **2018**, *456*, 379−389.

(49) Li, W.; Zhou, M.; Li, H.; Wang, K.; Cheng, S.; Jiang, K. A High Performance Sulfur-doped Disordered Carbon Anode for Sodium Ion Batteries. *Energy Environ. Sci.* **2015**, *8*, 2916−2921.

(50) Yang, J.; Zhou, X.; Wu, D.; Zhao, X.; Zhou, Z. S-Doped N-Rich Carbon Nanosheets with Expanded Interlayer Distance as Anode Materials for Sodium-Ion Batteries. *Adv. Mater.* **2017**, *29*, 1604108.

(51) Wang, T.; Wang, L. X.; Wu, D. L.; Xia, W.; Jia, D. Z. Interaction Between Nitrogen and Sulfur in Co-doped Graphene and Synergetic Effect in Supercapacitor. *Sci. Rep.* **2015**, *5*, 9591.

(52) Zhang, Y.; Guo, B.; Hu, L.; Xu, Q.; Li, Y.; Liu, D.; Xu, M. Synthesis of SnS nanoparticle-modified MXene ($Ti_3C_2T_x$) composites for enhanced sodium storage. *J. Alloy. Compd.* **2018**, *732*, 448−453.

(53) Shinde, S. S.; Sami, A.; Kim, D.-H.; Lee, J.-H. Nanostructured SnS-N-doped Graphene as an Advanced Electrocatalyst for The Hydrogen Evolution Reaction. *Chem. Commun.* **2015**, *51*, 15716−15719.

(54) Zhou, T.; Pang, W. K.; Zhang, C.; Yang, J.; Chen, Z.; Liu, H. K.; Guo, Z. Enhanced Sodium-Ion Battery Performance by Structural Phase Transition from Two-Dimensional Hexagonal-$SnS_2$to Orthorhombic-SnS. *ACS Nano* **2014**, *8*, 8323−8333.

(55) Wang, M.-S.; Wang, Z.-Q.; Chen, Z.; Yang, Z.-L.; Tang, Z.-L.; Luo, H.-Y.; Huang, Y.; Li, X.; Xu, W. One dimensional and coaxial polyaniline@tin dioxide@multi-wall carbon nanotube as advanced conductive additive free anode for lithium ion battery. *Chem. Eng. J.* **2018**, *334*, 162−171.

(56) Li, X.; Zhang, K.; Wang, M.; Liu, Y.; Qu, M.; Zhao, W.; Zheng, J. Dual Functions of Zirconium Modification on Improving the Electrochemical Performance of Ni-rich $LiNi_{0.8}Co_{0.1}Mn_{0.1}O_2$. *Sustainable Energy Fuels* **2018**, *2*, 413−421.

(57) Li, X.; Zhang, K.; Mitlin, D.; Yang, Z.; Wang, M.; Tang, Y.; Jiang, F.; Du, Y.; Zheng, J. Fundamental Insight Into Zr Modification of Li- and Mn-rich Cathodes: Combined Transmission Electron Microscopy and Electrochemical Impedance Spectroscopy Study. *Chem. Mater.* **2018**, *30*, 2566−2573.

(58) Shi, J.; Wang, Y.; Su, Q.; Cheng, F.; Kong, X.; Lin, J.; Zhu, T.; Liang, S.; Pan, A. N-S Co-doped C@SnS Nanoflakes/graphene Composite as Advanced Anode for Sodium-ion Batteries. *Chem. Eng. J.* **2018**, *353*, 606−614.

(59) Aravindan, V.; Gnanaraj, J.; Lee, Y.-S.; Madhavi, S. Insertion-type Electrodes for Nonaqueous Li-ion Capacitors. *Chem. Rev.* **2014**, *114*, 11619−11635.

(60) Weng, Z.; Li, F.; Wang, D.-W.; Wen, L.; Cheng, H.-M. Controlled Electrochemical Charge Injection to Maximize the Energy Density of Supercapacitors. *Angew. Chem., Int. Ed.* **2013**, *125*, 3810−3813.

(61) Thangavel, R.; Moorthy, B.; Kim, D. K.; Lee, Y.-S. Pushing the Energy Output and Cyclability of Sodium Hybrid Capacitors at High Power to New Limits. *Adv. Energy Mater.* **2017**, *7*, 1602654.

(62) Bhat, S. S. M.; Babu, B.; Feygenson, M.; Neuefeind, J. C.; Shaijumon, M. M. Nanostructured $Na_2Ti_9O_{19}$ for Hybrid Sodium-ion Capacitors with Excellent Rate Capability. *ACS Appl. Mater. Interfaces* **2018**, *10*, 437−447.

(63) Que, L.-F.; Yu, F. D.; Wang, Z. B.; Gu, D. M. Pseudocapacitance of $TiO_{2-x}$/CNT Anodes for High-performance Quasi-solid-state Li-ion and Na-ion Capacitors. *Small* **2018**, *14*, 1704508.

(64) Chen, Z.; Veronica, A.; Jing, W.; Yuewei, Z.; Meiqing, S.; Bruce, D.; Yunfeng, L. High-performance Supercapacitors Based on Intertwined CNT/$V_2O_5$ Nanowire Nanocomposites. *Adv. Mater.* **2011**, *23*, 791−795.

(65) Wang, X.; Li, G.; Chen, Z.; Augustyn, V.; Ma, X.; Wang, G.; Dunn, B.; Lu, Y. High-performance Supercapacitors Based on Nanocomposites of $Nb_2O_5$ Nanocrystals and Carbon Nanotubes. *Adv. Energy Mater.* **2011**, *1*, 1089−1093.

(66) Chen, Z.; Augustyn, V.; Jia, X.; Xiao, Q.; Dunn, B.; Lu, Y. High-performance Sodium-ion Pseudocapacitors Based on Hierarchically Porous Nanowire Composites. *ACS Nano* **2012**, *6*, 4319−4327.

(67) Lim, E.; Changshin, J.; Haegyeom, K.; Mok-Hwa, K.; Yeongdong, M.; Jinyoung, C.; Youngjin, Y.; Jongkook, H.; Kyoung-Su, H.; Kwang Chul, R. Facile Synthesis of $Nb_2O_5$@carbon Core-shell Nanocrystals with Controlled Crystalline Structure for High-power Anodes in Hybrid Supercapacitors. *ACS Nano* **2015**, *9*, 7497−7505.

(68) Chao, D.; Liang, P.; Chen, Z.; Bai, L.; Shen, H.; Liu, X.; Xia, X.; Zhao, Y.; Savilov, S. V.; Lin, J.; Shen, Z. X. Pseudocapacitive Na-ion Storage Boosts High Rate and Areal Capacity of Self-branched 2D Layered Metal Chalcogenide Nanoarrays. *ACS Nano* **2016**, *10*, 10211−10219.

DOI: 10.1021/acsami.9b14098
*ACS Appl. Mater. Interfaces* 2019, 11, 41363−41373